
Neuroblastoma Imaging Using a Combined CT Scanner–Scintillation Camera and ^{131}I -MIBG

H. Roger Tang, Angela J. Da Silva, Katherine K. Matthay, David C. Price, John P. Huberty, Randall A. Hawkins, and Bruce H. Hasegawa

Departments of Radiology and Pediatrics, University of California, San Francisco, California

High-dose administration of ^{131}I -metaiodobenzylguanidine (^{131}I -MIBG) continues to be a promising treatment for neuroblastoma. However, currently used methods of estimating ^{131}I -MIBG uptake in vivo may be too inaccurate to properly monitor patient radiation exposure doses. To improve localization and uptake measurements over currently practiced techniques, we evaluated different methodologies that take advantage of the correlated patient data available from a combined CT–scintillation camera imaging system. **Methods:** Serial CT and radionuclide scans of three patients were obtained on a combined imaging system. SPECT images were reconstructed using both filtered backprojection and maximum-likelihood expectation maximization (MLEM). Volumes of interest (VOIs) were defined on anatomic images and automatically correlated to spatial volumes in reconstructed SPECT images. Several radionuclide quantification methods were then compared. First, the mean reconstructed values within coregistered SPECT VOIs were estimated from MLEM reconstructed images. Next, we assumed that reconstructed activity in SPECT voxels were linear combinations of activities present in individual objects, weighted by geometric factors derived from CT images. After calculating the weight factors by modeling the SPECT imaging process with anatomically defined VOIs, least-squares fitting was used to estimate the activities within lesion volumes. We also estimated the lesion activities directly from planar radionuclide images of the patients using similar linearity assumptions. Finally, for comparison, lesion activities were estimated using a standard conjugate view method. **Results:** Activities were quantified from three patients having a total of six lesions with volumes ranging from 0.67 to 117 mL. Methods that used CT data to quantify lesion activities gave similar results for planar and tomographic radionuclide data. Estimating activity directly from mean VOI values in MLEM-reconstructed images alone consistently provided estimates lower than CT-aided methods because of the limited spatial resolution of SPECT. Values obtained with conjugate views produced differences up to fivefold in comparison with CT-aided methods. **Conclusion:** These results show that anatomic information available from coregistered CT images may improve in vivo localization and measurement of ^{131}I -MIBG uptake in tumors.

Key Words: correlated imaging; combined imaging system; absolute quantitation; SPECT; ^{131}I -MIBG

J Nucl Med 2001; 42:237–247

Neuroblastoma, the most common extracranial solid tumor in children, arises in the sympathetic nervous tissues and accounts for approximately 15% of all cancer deaths in young children (1). Metaiodobenzylguanidine (MIBG), a molecule functionally similar to the neurotransmitter norepinephrine, often localizes in sympathetic nervous tissues, including many neuroblastomas, most likely because of the same cellular uptake mechanism as norepinephrine (2).

Because MIBG localizes in the majority (80%–90%) of neuroblastomas, large injected doses of ^{131}I -MIBG can deliver high-energy, cytotoxic β radiation to cancer cells locally (3). However, because all tumors are biologically different, the uptake of MIBG in cancer cells varies. Pretreatment evaluation of patients can be performed through imaging studies using lower doses of ^{131}I -MIBG, or using ^{123}I -MIBG, a more convenient radioisotope for imaging because its 159-keV γ -ray emission is more optimally matched to the imaging characteristics of most scintillation camera systems. Post-treatment evaluation is equally important for therapy monitoring and for estimating the potential effects of radiation delivered to the patient. For instance, in therapy protocols involving a young population, it would be prudent to better understand the delayed effects of acute exposure. For both pre- and post-treatment evaluations, treatments can be optimized on the basis of estimated radiation doses delivered to patients and their tumors.

Although some researchers have begun using SPECT to determine the uptake of ^{131}I -MIBG (4), the conventional clinical technique used to measure the activity uptake is the method of conjugate planar views (5). However, phantom studies indicate high interobserver variability in uptake estimates with the standard conjugate view method as well as poor accuracy and precision for small tumors in the presence of high-activity background (6). In addition, we found that the tumor response after therapeutic administration of ^{131}I -MIBG, as determined by a change in tumor volume measured on CT images over time, correlated poorly with the tumor dose estimated using conjugate views (7). This result could occur if the biologic response of the tumor to radiation is unrelated to the anatomic response because of differential radiosensitivity, necrosis, or scar. However,

Received Jan. 5, 2000; revision accepted Sep. 14, 2000.

For correspondence or reprints contact: H. Roger Tang, PhD, UCSF Physics Research Laboratory, 389 Oyster Point Blvd., Suite 1, South San Francisco, CA 94080.

measurement of uptake activity may not be sufficiently accurate using the method of conjugate views. To reduce dose uncertainties caused by poor uptake estimation, it is important to develop accurate measurement tools and methods.

To improve radionuclide uptake measurements, we are spatially correlating radionuclide data to CT images. To accomplish this, we use an imaging system that combines a commercial CT scanner with a single-head scintillation SPECT camera using a common patient table (8). CT scans and radionuclide scans are acquired in succession by a simple translation of the imaging table, minimizing registration uncertainty caused by patient repositioning and shifts in internal anatomy. Volumes of interest (VOIs) defined in one image space (e.g., CT) are easily transferred into the other image space (e.g., SPECT) using the known spatial relationship of the datasets. In addition, a spatially registered anatomic CT image, when scaled for the photon energy of the radionuclide, provides an estimate of the attenuation distribution required for the quantitative correction of radionuclide data.

In this article, we describe the measurement methods that have been developed for a combined CT–scintillation camera imaging system for the absolute *in vivo* measurement of activity concentration in neuroblastoma patients. Individual patient examples will illustrate some of the practical difficulties associated with the different measurement methods, especially whether or not tumor outlines drawn on CT images may be useful for the extraction of quantitative data from coregistered radionuclide images.

MATERIALS AND METHODS

System Description

Figure 1 is a diagram of the combined CT–scintillation camera imaging system. Because the two systems are colinear and fixed, the image spaces of each system are spatially registered using simple transformation matrices. We developed a method to determine the spatial transformation matrices for the prototype imaging system using small markers filled with a potassium phosphate (K_2HPO_4) and ^{99m}Tc -pertechnetate solution to make them visible in both CT and radionuclide images. With this method, several markers are tomographically scanned on both systems using known imaging geometries. A linear least-squares approach is then used to determine the optimal transformation matrix for each

imaging geometry after measuring the location of each marker in each set of reconstructed images (8).

The registration accuracy of the system (0.0 ± 0.4 mm) is well within the pixel sizes of both standard reconstructed CT images (0.9375 mm) and reconstructed radionuclide images (4.32 mm). The registration errors are slightly larger in the axial dimension because of coarser sampling with the CT scanner.

Patient Scans

Three patients, who had clinically confirmed recurrent neuroblastoma and were participating in an ^{131}I -MIBG therapy protocol at the University of California, San Francisco (UCSF), were selected for additional quantitative imaging studies using the combined CT–scintillation camera system. Informed consent was obtained from both parents or guardians. The imaging protocol was reviewed and approved by the UCSF Committee on Human Research. Patients requiring anesthesia or patient restraints to prevent motion during scanning were excluded from this imaging study.

For their MIBG therapies, the patients were infused with 11.8–29.6 GBq (320–800 mCi) ^{131}I -MIBG through an intravenous line using a syringe pump over a period of ~ 2 h (3). The injected activity was ~ 670 MBq (18 mCi) per kilogram of body mass. As part of their therapy protocol, the patients were imaged at UCSF using standard conjugate planar views (5) on the third and seventh days after their MIBG infusions to estimate the total radiation dose to their neuroblastomas. An additional measurement was made on these patients using the combined CT–scintillation camera imaging system 5 d after their initial therapy infusion. No special patient restraints were necessary, but markers containing ^{99m}Tc and K_2HPO_4 were placed on some patients to aid in image registration in case they moved during imaging. Patients were also allowed to breathe naturally throughout all the scans, and their arms were left in the same position (at their sides) for both CT and radionuclide imaging.

No iodinated contrast agents (oral or intravenous) were used in the first two patients. CT scans were obtained with the GE9800 Quick (General Electric Medical Systems, Milwaukee, WI) using a 140-kVp tube potential, a 70-mA tube current, 2-s/slice scans, and 3-mm axial slice collimation and spacing over the extent of the known tumor region. The projection data were reconstructed onto 512×512 pixel, 48-cm-diameter field-of-view images using the scanner's standard reconstruction kernel and then transferred to a workstation for further processing. The total CT scan time was <10 min.

After the CT scans, the patients remained on the imaging table without moving, were translated into the scintillation camera gantry, and were imaged with a 600XR/T detector (General Electric)

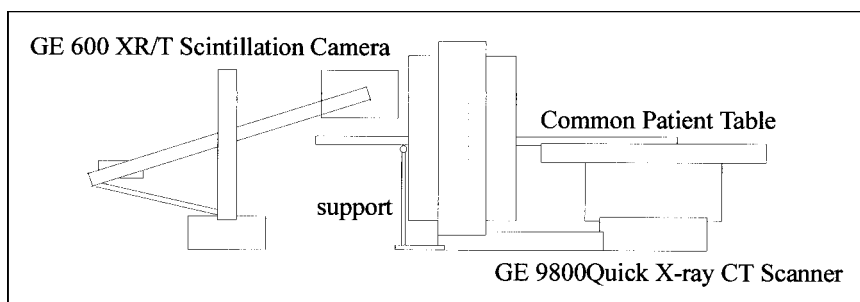


FIGURE 1. Combined CT–scintillation camera imaging system.

using a high-energy general-purpose collimator ([HEGP] Nuclear Fields, The Netherlands). First, standard conjugate planar views were obtained for 2.5–3 min per view to obtain $>1 \times 10^6$ counts per planar image using a 15% energy window at 364 keV. For attenuation compensation of the conjugate view planar measurements, calibrated point sources of ^{131}I were placed on the surfaces of the patients at body locations with roughly equivalent total attenuation as the tumor sites. Although these locations were selected by an experienced nuclear medicine physician, the attenuation factors determined by these point sources may be inaccurate, leading to inaccurate estimates of the in vivo activity. For each patient, after the four conjugate planar views were acquired (two anterior and two posterior planar images, each with and without the calibrated ^{131}I point source), tomographic scans were obtained over 360° using 64 stops at 10 s/stop at a known radius of rotation (24.0 cm for patient 1 and 25.1 cm for patient 2) and using a 15% energy window at 364 keV. For radionuclide scans that included $^{99\text{m}}\text{Tc}/\text{K}_2\text{HPO}_4$ -filled markers attached to the patient, an additional 15% energy window was placed at 140 keV to detect the 140-keV γ -ray of $^{99\text{m}}\text{Tc}$. The total scan time was approximately 35–40 min for the planar and tomographic scans.

The third patient was scanned with both oral and intravenous iodine contrast agents to help better delineate tumor boundaries. In addition, the third patient was scanned in a slightly different order. Conjugate planar imaging was performed first so that the camera and patient could be repositioned to obtain planar images as close as possible to the patient's body to maximize the planar image resolution. A total of 800 mL oral contrast (Hypaque; Nycomed, Princeton, NJ; 10 mg/400 mL) was ingested by the patient in small amounts and at small intervals over the hour before the CT scan; the last 100 mL were ingested just before the start of CT imaging. During the CT scan, 120 mL intravenous nonionic iodine contrast (Omnipaque; Nycomed; 300 mg/mL) were syringe injected by hand through a central line at ~ 1 –2 mL/s. Forty seconds after the start of the intravenous contrast injection, CT imaging began using a 140-kVp tube potential, a 100-mA tube current (a higher tube current was used because this patient was larger), and a 2-s/slice scan time. A total of 50 5-mm-thick, 5-mm-spaced axial slices were obtained. The thicker axial slices were necessary to allow scanning of the entire tumor region in a short enough time to permit visualization of the intravenous contrast medium in the blood pool. This procedure may have affected the tumor volume measurement. Immediately after CT scanning, the intravenous lines for contrast injection were flushed with saline (taking approximately 2 min) without moving the patient. After the patient was translated to the scintillation camera, a single anterior planar image was acquired for 3 min, immediately followed by tomographic scanning at 20 s/stop for 64 stops over 360° at a radius of rotation of 24.3 cm.

To calibrate the reconstructed image values to physical units (MBq/mL), a 15-cm-diameter cylindrical tank containing a known uniform activity concentration of ^{131}I of 14.2 kBq/mL (0.385 $\mu\text{Ci}/\text{mL}$) was also imaged in the combined system using acquisition techniques similar to those of the patient scans.

Data Analysis

VOIs. Several VOIs were defined directly on the CT scans. First, for each patient, the tumor boundaries were defined with the aid of a pediatric radiologist. For the abdominal scans, the liver volume was also defined as a separate VOI. Pulmonary regions were

segmented using a CT number threshold of 800 Hounsfield units (HU). Finally, the rest of the body tissues with CT numbers > 800 HU, excluding the liver and tumors, were defined as a general background VOI. After VOIs were defined directly on the CT images, they were transferred to scintillation camera space using the known spatial relationship between datasets.

Image Reconstruction. After image registration, the CT images were converted to correlated attenuation distributions by scaling the CT data using K_2HPO_4 (bone) calibration factors and iodine calibration factors as described in a previous study (9). Using the registered patient-specific attenuation distribution, the tomographic emission data were reconstructed with the maximum-likelihood expectation maximization (MLEM) algorithm (10). Two variations of the algorithm were used. One version used 30 iterations but did not model the resolution effects of the HEGP collimator (noncollimator-compensated MLEM) to reduce computer processing time. The second version used 200 iterations and modeled the collimator using a distance-dependent blurring collimator model for the HEGP collimator in an attempt to recover resolution loss (11,12), thereby requiring much longer computer processing time. The emission data were also reconstructed using filtered backprojection (FBP) with a Butterworth filter of power 8 and cutoff frequency of 0.35 Nyquist. In all cases, no postreconstruction filtering was applied.

Standard Tomographic Image Analysis. We first used the coregistered CT VOIs defined manually as described above to delineate physical tumor boundaries in the SPECT images. The mean activity concentration in each tumor VOI was estimated (the mean VOI, or MVOI estimate) using the coregistered CT tumor VOIs overlaid onto the reconstructed MLEM images (13). This technique represents a method that estimates the activity concentration from reconstructed SPECT images directly.

Tomographic Analysis Using Templates. Previous phantom studies showed that standard MVOI measurements were inaccurate for smaller lesions because of the limited spatial resolution of SPECT (13). These errors are difficult to correct completely using radionuclide data alone, even after attenuation correction and compensation for the effects caused by collimation. Therefore, we took advantage of the a priori structural information available from the coregistered tumor VOIs to help overcome these resolution errors. After assuming that the activity concentration within each VOI was uniformly distributed, VOIs were defined for the lesions and other anatomic structures (e.g., lung, liver, and "background" tissues) adjacent to the lesions that could affect (blur into) the radionuclide object of interest. After VOIs were defined for each object on the CT images and transformed to scintillation camera space, the correlated VOIs were converted into three-dimensional templates of unit activity concentration. Projection data were calculated for these unit activity distributions using models for photon attenuation and the nonideal collimator for the different views acquired of the object during actual tomographic imaging. After the template projection data for the lesions and the neighboring objects were generated, the templates were reconstructed with the same reconstruction algorithms used for reconstructing the emission data (MLEM and FBP). This process produced reconstructed templates, representing the effects of both the imaging and reconstruction process. An overview of the process is outlined in Figure 2.

The reconstructed templates were then used in two ways. First, we used the reconstructed templates to correct the reconstructed SPECT images on a voxel-by-voxel basis. The reconstructed SPECT images were rescaled directly by dividing the appropriate

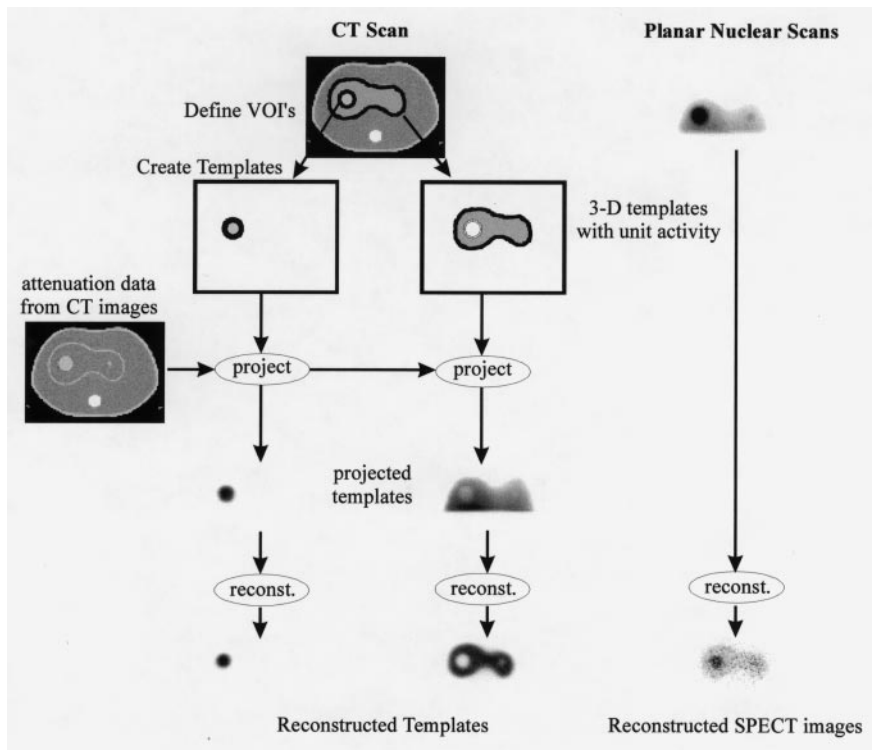


FIGURE 2. Overview of template projection reconstruction process.

tumor activities on a voxel-by-voxel basis with the corresponding reconstructed template. The corrected mean activity concentration in each tumor VOI was then estimated as follows:

$$\bar{\rho}_{\text{corrected}} = \frac{1}{n_{\text{VOI}}} \sum_{i \in \text{VOI}} \frac{\rho(i)}{f_{\text{object}}(i)}, \quad \text{Eq. 1}$$

where the index i identifies each voxel in the VOI ($i = 1 \dots n_{\text{VOI}}$) and n_{VOI} is the number of voxels in the tumor VOI. The values $\rho(i)$ and $f_{\text{object}}(i)$ are the reconstructed activity concentration and reconstructed tumor template in the i th voxel of the object VOI. We will refer to this method as template-correction. This method was verified using both phantom (12,14,15) and animal (16,17) experiments. Conceptually similar methods have been applied to correct for resolution errors in PET of the brain using correlated MR images (18).

For our next method, we assumed that reconstructed images are linear combinations of objects with different activity concentrations within the reconstructed image. Therefore, the value in each voxel of the reconstructed SPECT images, $\rho(i)$, can be represented as:

$$\rho(i) = \sum_{m=1}^M A_m f_m(i), \quad \text{Eq. 2}$$

where there are M total objects with a uniform activity concentration of A_m in the m th object. Therefore, each reconstructed voxel is a linear combination of the activities from the M different objects weighted by their fractional contributions to the reconstructed voxel i . To estimate the activity concentration in each lesion, we fit for the activity concentrations (A_m) that minimized the least-square error:

$$\chi^2 = \sum_{i=1}^{n_{\text{VOI}}} \left[\rho(i) - \sum_{m=1}^M A_m f_m(i) \right]^2. \quad \text{Eq. 3}$$

Again, the values $\rho(i)$ and $f_m(i)$ are the reconstructed activity concentration and m th reconstructed tumor template value in the i th voxel of the object VOI. We will refer to this as a tomographic least-squares method (LS-ML or LS-FBP). This method was also verified using phantom experiments (12,14). Again, conceptually similar methods have been applied in PET of the brain using correlated MR images (19).

Planar Analysis Using Templates. The tumor activity concentrations were estimated directly from planar emission data using a weighted linear least-squares (WLS) method, as described in previous article (9). In summary, we estimated the activity concentrations (A_m) using a weighted least-squares fit to the following relationship:

$$p(d) = \sum_{m=1}^M A_m \phi_m(d), \quad \text{Eq. 4}$$

where $p(d)$ is the number of counts in detector bin d of the planar emission data, A_m is the activity concentration in the m th object (to be estimated), $\phi_m(d)$ is the relative physical contribution from the m th object into the d th ($d = 1 \dots D$) detector bin calculated from the projected CT-defined templates, and M is the total number of objects. The uncertainty for each $p(d)$ measurement was assumed to follow Poisson statistics (i.e., $\sigma(d) = \sqrt{p(d)}$). Therefore, the least-squares minimization is of the following form:

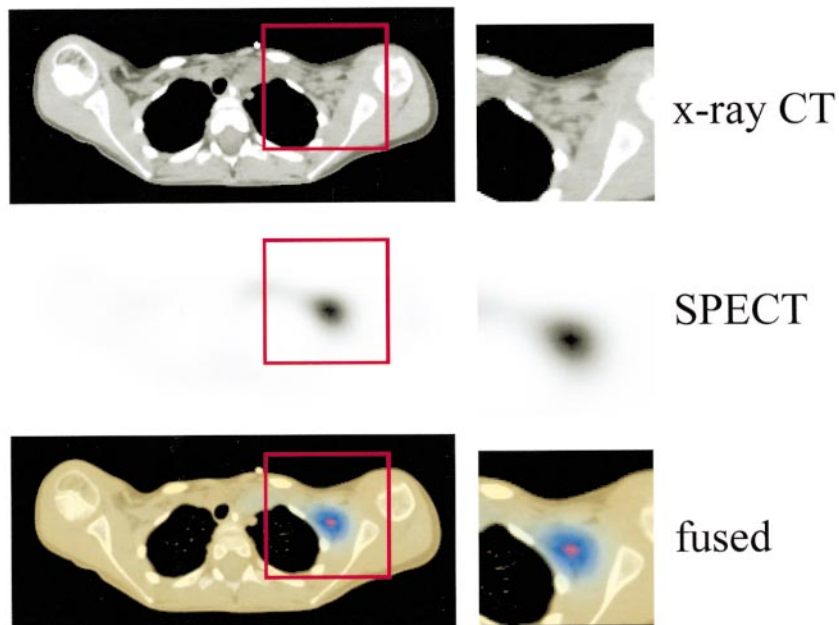


FIGURE 3. Example of fused image available from combined CT–scintillation camera imaging system. CT image is shown along with spatially correlated SPECT image indicating ^{131}I -MIBG uptake in lymph node in patient’s left axilla.

$$\chi^2 = \sum_{d=1}^D \left[\frac{p(d) - \sum_{m=1}^M A_m \phi_m(d)}{\sqrt{p(d)}} \right]^2. \quad \text{Eq. 5}$$

We will refer to this as a planar WLS. A theoretic description of this concept was presented by Formiconi (20). This method was also verified using phantom experiments (9,12).

Standard Conjugate View Analysis. For comparison purposes, a nuclear medicine physicist evaluated the conjugate view planar data using a standard conjugate view method (5). Region-of-interest (ROI) outlines were drawn around the tumors on the planar radionuclide images, and estimates of the nontumor activity (background) within the tumor ROIs were made by drawing additional ROIs immediately adjacent to the tumor ROIs. The total tumor attenuation was determined by drawing ROIs around the ^{131}I point source of known activity for both the anterior and the posterior views in those scans with the point source present and subtracting the background counts from matched ROIs on the views with the point source removed. The tumor activity, A (MBq), was calculated using the following equation:

$$A = \left(\frac{(I_A - B_A)(I_P - B_P)}{(S_A - SB_A)(S_P - SB_P)} \right)^{1/2} \sigma, \quad \text{Eq. 6}$$

where I_A and I_P are the counts from planar ROIs surrounding the tumor on the anterior and posterior camera views, respectively; B_A and B_P are the estimates of the overlap (background) counts in the I_A and I_P measurements, respectively (normalized for the number of pixels in the ROIs); σ (MBq) is the activity of the known, calibrated ^{131}I source placed on the patient; S_A and S_P are the counts from the known, calibrated source in ROIs on the anterior and posterior camera views, respectively; and SB_A and SB_P are the background counts in the same ROIs as for the point source but on planar scans with the source removed. The activity concentration was calculated by dividing the total estimated activity by the CT-defined volume of the tumor.

RESULTS

CT-Defined Volumes

The tumor volumes of interest were defined on the CT scans for each of the tumors as described previously. For large abdominal tumors (patients 1 and 3), the tumor boundaries were difficult to define, even with the aid of iodinated contrast agents. Involved lymph nodes were much easier to localize, especially if overlaid with correlated reconstructed SPECT scans. Figure 3 shows an example of such an image overlay, revealing localization of ^{131}I -MIBG in an involved lymph node in a patient’s left axilla.

In patient 1, the primary tumor was located in the abdomen surrounding the descending aorta. On planar ^{131}I -MIBG images of patient 1, there appear to be three individual tumors (Fig. 4). One main mass was just surrounding the descending aorta, and a small nodal mass was connected to it by a bridge of tissue. A separate, small nodal mass was also detectable just inferior to the main mass. We treated the two semiconnected masses as a single large tumor mass, giving us essentially one large and one small tumor mass. The resulting CT-derived volumes were 48.5 and 2.1 mL.

In patient 2, the main lesion being imaged was a cancer-involved lymph node near the left clavicle. Planar ^{131}I -MIBG images show two additional, smaller involved nodes (Fig. 4). One node was too close to the primary lesion to be separable on nuclear and CT scans. Therefore, those two masses were considered as one volume. The other, independent, enlarged lymph node was located near the left axilla. The resulting CT-derived volumes were 12.7 and 0.67 mL.

In patient 3, as in patient 1, the primary tumor was located in the abdomen adjacent to the descending aorta. However, because of previous surgery in the tumor region,

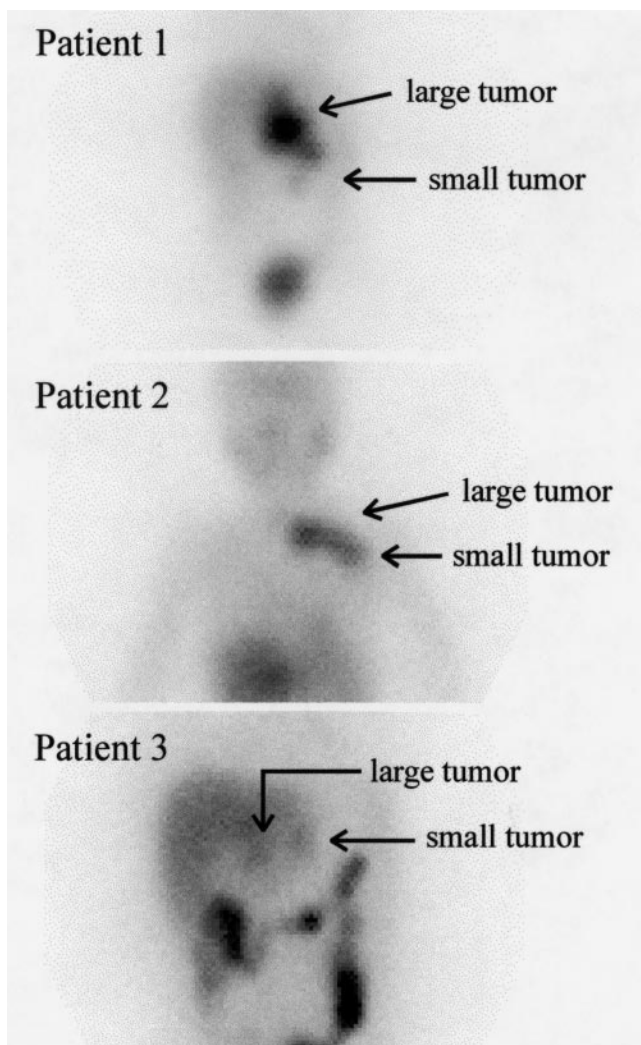


FIGURE 4. Anterior planar ^{131}I -MIBG scans of three neuroblastoma patients. Patient 1 shows two separate lesions in abdomen along with normal liver uptake (left side of image) and excreted bladder activity (lower portion of image). Patient 2 shows one lesion in left clavicle and one near left axilla along with liver uptake (lower portion of image) and diffuse low-level background tissue uptake. Patient 3 shows two (faint) lesions in abdomen along with normal liver uptake (left side of image) and intense activity in large bowel.

the CT scans were difficult to interpret. The surgical bed was relatively easy to outline, but it was difficult to distinguish between viable tumor and surgical scar. Because of this, the defined tumor volume was complex in shape. However, two separable masses on the nuclear images were definable on the CT images once the CT images and reconstructed emission data were correlated and examined (Fig. 4). The accuracy of the CT-defined tumor volumes in patient 3, however, remains unclear. The estimated CT-derived volumes were 117 and 1.3 mL.

Summary of Quantitative Analysis Methods

The resulting activity concentrations estimated using the different analytic methods are summarized in Table 1. For

comparison, the activity concentrations estimated using the standard conjugate view method are also presented in Table 1. The following sections discuss the results of the different analytic methods individually.

Standard Tomographic Image Analysis

In comparison with noncollimator-compensated MLEM reconstruction, MLEM reconstruction with collimator compensation led to higher estimates of the tumor activity concentration with the mean VOI estimate, as well as improved visual image quality. This result was consistent with the results of previous experimental phantom studies using $^{99\text{m}}\text{Tc}$ (12,13).

Figure 5 shows correlated slices through a central region of patient 1 for the three reconstruction methods (FBP, MLEM, and MLEM with collimator compensation). For both the large (48.5 mL) and small (2.1 mL) lesions, the MVOI estimates were higher by a factor of 2 using the MLEM reconstructions that modeled the collimator.

Figure 6 shows correlated slices through a central region of each of the involved masses in patient 2 using the three reconstruction methods. For both the large (12.7 mL) and small (0.7 mL) lesions, the MVOI estimates were higher by a factor of 3–4 using the MLEM reconstructions that modeled the collimator.

Figure 7 shows correlated slices through a central region of patient 3 for the three reconstruction methods. Using collimator compensation in the MLEM reconstruction, the MVOI estimate was 50% higher for the large (117 mL) lesion, whereas the MVOI estimate was 2.5 times higher for the small (1.3 mL) lesion.

Tomographic Analysis Using Templates

Using the reconstructed templates to rescale the reconstructed SPECT images on a voxel-by-voxel basis with Equation 1 (template-correction) led to estimated concentrations that were higher than those values estimated by taking the mean reconstructed activity concentration within the tumor VOIs. However, because these template-corrected estimates accounted for only the effects caused by limited SPECT spatial resolution in the target lesion and did not include compensation for activity “blurring in” from neighboring regions, the results represented an upper bound for the activity concentration in the lesions of interest.

Least-squares fitting using the reconstructed templates and reconstructed SPECT images also estimated concentrations that were higher than the mean activity concentrations but were smaller than the mean concentrations estimated after template correction. In addition, the least-squares estimates were similar using either MLEM or FBP.

Planar Analysis Using Templates

In all patients, WLS fitting of the projected templates and the planar emission data produced higher concentration estimates than using the MVOI measurement on the reconstructed SPECT images (again, because of re-

TABLE 1
Tumor Volume Measurement Results for Three Patients Using Different Measurement Methods

Patient no.	Method*								
	CT (mL)	CV	MVOI		LS		TC		WLS
			No coll	W/coll	ML	FBP	ML	FBP	
Patient 1									
Large	48.5	1.77	0.440	0.914	1.22	1.22	1.59	1.54	1.29
Small	2.1	0.67	0.135	0.254	1.27	0.98	3.34	2.89	0.400
Patient 2									
Large	12.7	0.318	0.0770	0.255	0.335	0.327	0.470	0.429	0.329
Small	0.67	2.57	0.0992	0.370	3.625	3.50	6.845	5.11	3.922
Patient 3									
Large	117	0.0348	0.0433	0.0614	0.0681	0.0755	0.147	0.139	0.0722
Small	1.3	0.705	0.0592	0.148	1.53	1.75	3.13	2.94	1.132

*Measurements in MBq/mL unless otherwise noted.

CV = standard conjugate views; MVOI = mean volume of interest, with and without compensation for collimator (coll); LS = least-squares fitting with reconstructed SPECT data and templates; TC = template correction with reconstructed SPECT data and templates; WLS = planar weighted least-squares fitting using planar emission data and projected templates; ML = maximum-likelihood expectation maximization reconstruction; FBP = filtered backprojection reconstruction.

sidual SPECT spatial resolution errors in the MVOI estimate) and estimated smaller concentrations than using template correction of the reconstructed SPECT data. In fact, the activity concentrations estimated with planar

WLS fitting were similar to the activity concentrations estimated with least-squares fitting of the reconstructed templates and SPECT images, especially for the larger lesions.

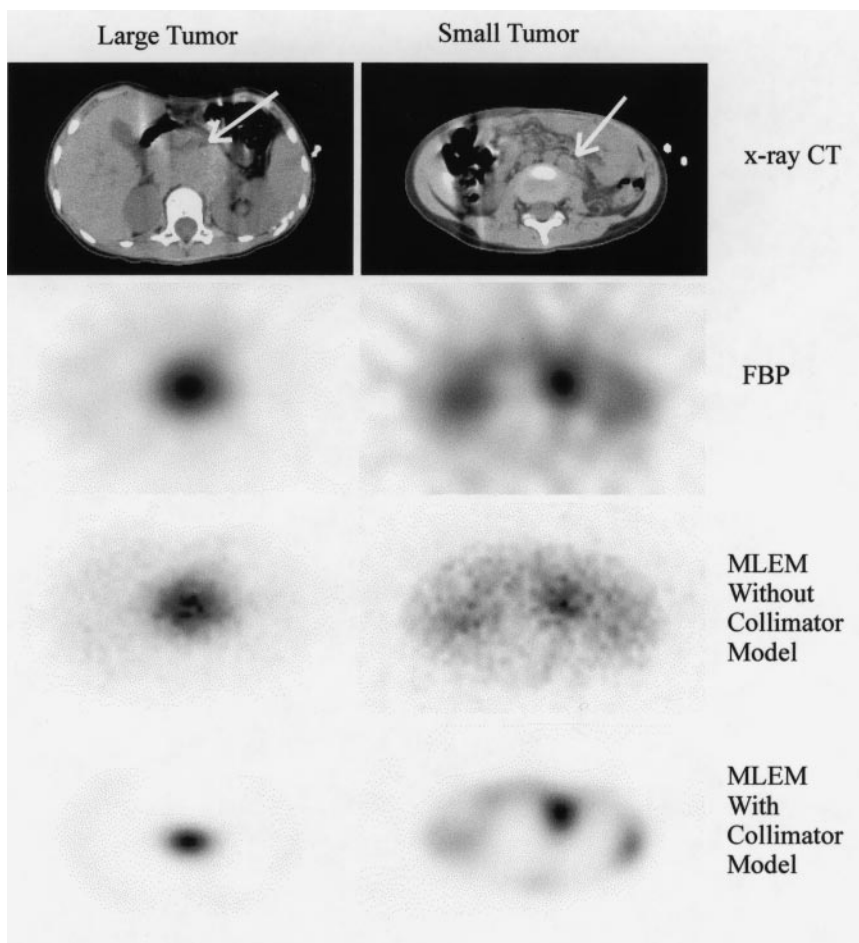


FIGURE 5. Coregistered CT and reconstructed SPECT images of patient 1.

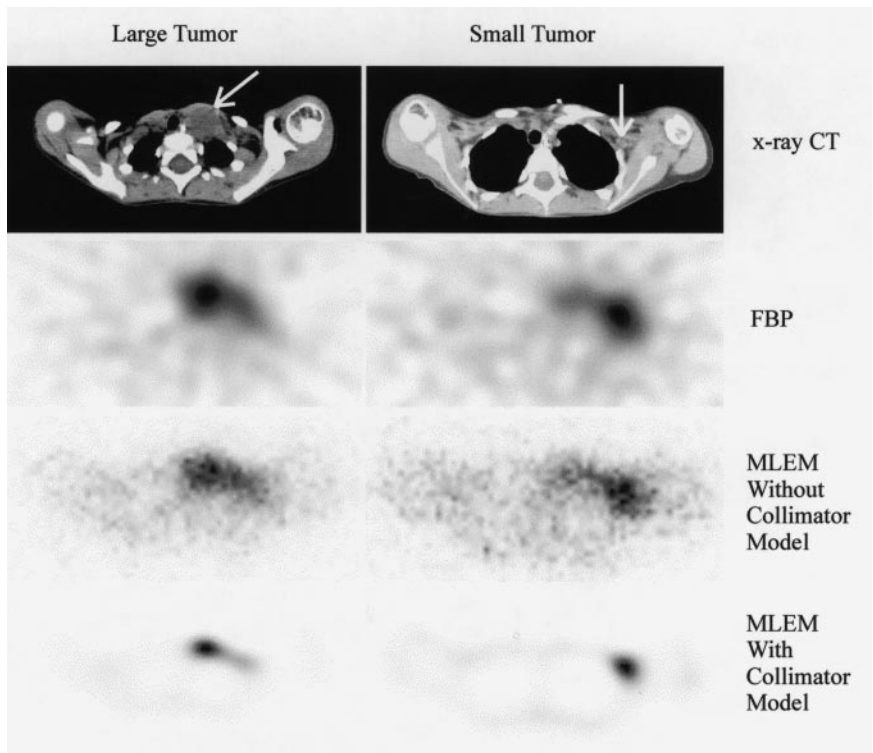


FIGURE 6. Coregistered CT and reconstructed SPECT images of patient 2.

DISCUSSION

From our experience with experimental phantoms (12,13), we expected the MVOI technique to underestimate the activity concentration in any case, regardless of the collimator model used in the reconstruction, simply because of resolution effects that are difficult, if not impossible, to overcome. Compensation for the collimator in the iterative reconstruction algorithm may not be enough to “recover” the activity of the small objects. Therefore, we believe that the reconstructed mean activity concentrations obtained with this technique are lower bounds for the actual activity concentrations in these patients (assuming that the CT-defined volume is an accurate assessment of the tumor volume).

Correcting the activity concentrations by dividing the reconstructed SPECT images on a voxel-by-voxel basis with the reconstructed object templates usually produced the highest activity concentration estimates of all of the methods. This template correction essentially rescales the activity concentration estimate with a shape- and size-dependent “recovery coefficient,” which is often necessary when estimating the activity concentration of objects near or below the resolution limit of the radionuclide imaging system (21). When no adjustment for nonlesion activity is performed, the result should represent an upper bound on the activity concentration within the volume (assuming that the CT-derived volume is an accurate assessment of the tumor volume). That is to say, template correction without background subtraction accounts for the blurring (spill-out) of the tumor activity, but scales up the spill-in activity from

the nontumor regions by the same factor, leading to an overestimate of the activity concentration. Therefore, if the CT-derived volume is accurate, it is reasonable to assume that the actual activity concentration in the object is smaller than the result estimated by template correction of the images (without background subtraction). Further correction for the blurring in of neighboring activity is necessary to estimate the actual mean activity concentration. A possible estimate would be through a modification of Equation 1:

$$\bar{\rho}_{\text{corrected}} = \frac{1}{n_{\text{VOI}}} \sum_{i \in \text{VOI}} \frac{\rho(i) - \bar{b}_{\text{est}} \cdot f_{\text{background}}(i)}{f_{\text{object}}(i)}, \quad \text{Eq. 7}$$

where \bar{b}_{est} is an estimate of the nontarget activity concentration, and $f_{\text{background}}(i)$ is the i th voxel in the reconstructed template of a neighboring nontarget, or background, VOI. As in Equation 1, $\rho(i)$ and $f_{\text{object}}(i)$ are the reconstructed activity concentration and reconstructed tumor template in the i th voxel of the VOI, respectively. The major difficulty lies in accurately estimating the value of the neighboring activity concentration, \bar{b}_{est} .

The results of the planar measurement using WLS and the least-squares estimate using MLEM and FBP reconstructed images were remarkably similar for the large tumors but showed larger variations for the smaller lesions. These methods are also based on the template projection concept in which VOIs are defined on the CT image and the expected template projections are calculated from CT-defined volumes. Here, the activity concentration estimates are

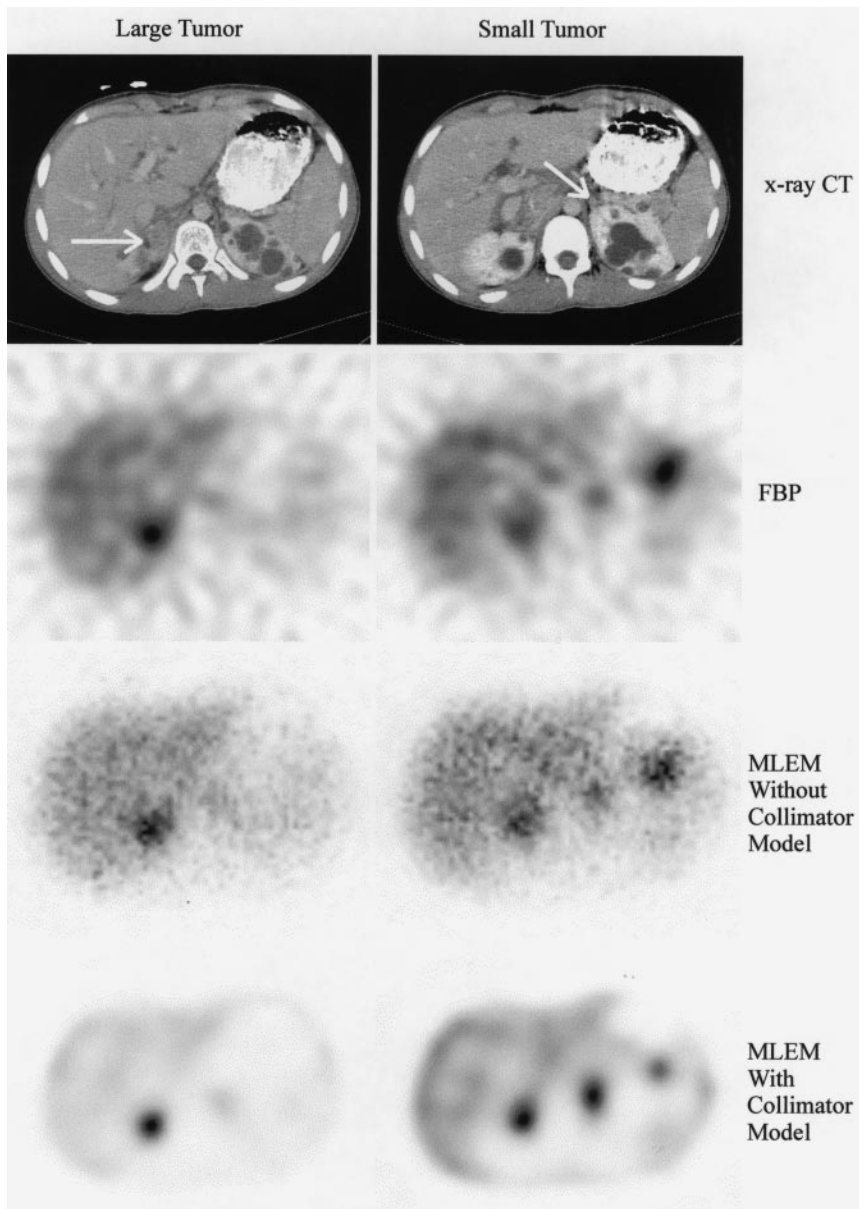


FIGURE 7. Coregistered CT and reconstructed SPECT images of patient 3. In images on right, central focus is small lesion that does not appear to anatomically correspond to left adrenal; left focus is part of large lesion; and right focus is part of bowel uptake.

based strictly on the geometric relationships between the assumed uniform distributions of activity and the measured planar or reconstructed SPECT data and least-squares fitting.

In this study, we modeled only the patient-specific attenuation and collimator response in our template projection process; however, other physical models are readily incorporated, including models for scatter, patient motion, and pharmaceutical kinetics. Although it is computationally expensive to include these effects in an iterative reconstruction for SPECT (and still not achieve accurate representations of the activity distribution), computing these effects once for individual CT-defined templates may be practical. When using the template projection concept for SPECT, the measurement accuracy probably does not depend as strongly on such free parameters as iteration number (MLEM) or recon-

struction filter (FBP) because both templates and data undergo the same imaging and reconstruction processes. Therefore, it is not necessary to produce images of high visual quality to measure the activity concentration accurately.

Despite our goal of improving the anatomic definition precision using the high-resolution images available from CT scanning, in our experience the dominant source of measurement error may still be CT volume uncertainty. The task of delineating the tumor boundaries was especially tedious and difficult for the largest tumors, whereas for smaller nodes, the boundaries were generally much clearer. As an example of this uncertainty, pretreatment CT scans of the same patients were obtained within 3 wk before our CT scans. These pretreatment CT scans were also analyzed to define the tumor volumes. In these cases, tumor VOIs were

TABLE 2
Comparison of CT-Derived Tumor Volumes for Separate
CT Scans and Analyses of Patients

Patient no.	Our CT-defined volume (mL)	Independent CT-defined volume (mL)
1	48.5	63.4
2	12.7	13.3
3	116.8	85.7

defined by hand and measured by scanning the hand-drawn VOIs into a computer. The sums of the voxels within each VOI were scaled by the CT slice width and pixel size to finally obtain physical volumes. Table 2 compares the tumor volumes measured from our CT scans with volume measurements from this separate measurement method for the three patients discussed (only the larger tumor volumes were estimated). The results indicate large differences in the volume measurement. Of course, these differences could be attributed to the fact that our CT scans were performed 5 d after the start of treatment and 3 wk after the pretreatment CT scans. However, we suspect that anatomic changes caused by the time difference between the two scans were not a large factor in the measurement difference, but the difficulty was in consistently judging tumor boundaries using different approaches.

From a practical imaging perspective, we found that the entire combined set of examinations took <1 h because the time between CT and radionuclide scans was small. As a result, all of the patients were able to tolerate the combined imaging method without difficulty. Therefore, we do not believe that additional restraints or sedation is necessary to ensure proper image registration.

Although the measurement techniques were developed using the combined CT-scintillation camera imaging system, these methods are not necessarily limited to that system. As researchers continue to develop better methods for the spatial registration of anatomic and radionuclide data, these methods may be applied to data acquired on separate imaging systems. In addition, the concepts are not restricted to CT and SPECT images. Others have investigated the use of such template methods using correlated MRI and PET images of the brain (18,19,22).

From a scientific perspective, the important question is whether the proposed measurement techniques are more accurate in measuring the tumor activity concentration than the currently practiced standard conjugate view method. The measurement accuracy was impossible to determine in this study, because we could not excise the tumor immediately after imaging to measure its activity. However, in our experience, phantom studies using different simulated "tumor" sizes and a variety of background activities have shown that the proposed CT-assisted techniques are usually more accurate in comparison with a standard conjugate view technique (9,12,23). Although these experimental

phantom studies and additional animal studies (17) have shown the accuracy of these CT-assisted measurement techniques, individual patient examples provided additional perspectives into the actual application of the different techniques, the results of which at least could be compared directly with the results of the standard conjugate view measurement method. We know at least that the measurement results differed in some tumors, providing evidence that the proposed measurements were offering a different, although not necessarily better, activity estimate in some cases. We have to infer from the results of our previous phantom and animal experiments that these proposed CT-assisted measurement techniques are potentially more accurate than our standard conjugate view method.

CONCLUSION

We examined the practical, clinical application of several activity measurement methods developed for a combined CT-scintillation camera imaging system. Several important results were apparent from these initial scans. First, patient compliance for the combined scans was excellent because of the relatively short scan times and short times between scans, reducing the necessity of placing additional fiducial markers or restraining the patient for the purpose of image registration. Second, methods that defined anatomic VOIs on CT images and that estimated the activity concentrations directly from planar and tomographic scans resulted in similar measurements. In addition, these results were similar to those achieved with a standard conjugate view technique for larger lesions in most cases, but they were quite different in some cases, especially for smaller lesions. A lower bound on the activity concentration can be estimated from the mean reconstructed activity concentration in a tumor VOI. Similarly, an upper bound on the activity concentration can be estimated by correcting the reconstructed SPECT images for spill-out by dividing the reconstructed values in a tumor VOI with the reconstructed anatomic template of the tumor. Finally, possibly the largest source of quantitative uncertainty is the CT-defined volume, especially for large, complex tumors. Assessment of the clinical use of any of the measurement techniques requires further investigation.

ACKNOWLEDGMENTS

The authors thank GE Medical Systems for the generous equipment grant that made this work possible. This research was performed during the tenure of an Established Investigatorship from the American Heart Association for Bruce Hasegawa. The authors also wish to thank Michael Zetina for help with the CT scans, Janet Veatch for help with patient handling, and Wendy Patton for aid in defining tumor boundaries.

REFERENCES

1. Shulkin BL, Shapiro B. Current concepts on the diagnostic use of MIBG in children. *J Nucl Med.* 1998;39:679-688.

2. Sisson JC, Shapiro B, Meyers L, et al. Metaiodobenzylguanidine to map scintigraphically the adrenergic nervous system in man. *J Nucl Med.* 1987;28:1625–1636.
3. Matthay KK, DeSantes K, Hasegawa B, et al. Phase I dose escalation of ¹³¹I-metaiodobenzylguanidine with autologous bone marrow support in refractory neuroblastoma. *J Clin Oncol.* 1998;16:229–236.
4. Koral KF, Zasadny KR, Kessler ML, et al. CT-SPECT fusion plus conjugate views for determining dosimetry in iodine-131-monoclonal antibody therapy of lymphoma patients. *J Nucl Med.* 1994;35:1714–1720.
5. Shulkin BL, Sisson JC, Koral KF, Shapiro B, Wang XH, Johnson J. Conjugate view gamma camera method for estimating tumor uptake of iodine-131 metaiodobenzylguanidine. *J Nucl Med.* 1988;29:542–548.
6. Tang HR, Brown JK, Hasegawa BH. An x-ray CT-assisted method for radionuclide activity measurement using planar views. In: Nalcioglu O, ed. *1997 IEEE Nuclear Science Symposium Conference Record.* Albuquerque, NM: IEEE; 1997:1620–1624.
7. Matthay KK, Huberty JP, Hattner RS, et al. Efficacy and safety of [¹³¹I]metaiodobenzylguanidine therapy for patients with refractory neuroblastoma. *J Nucl Biol Med.* 1991;35:244–247.
8. Blankespoor SC, Wu X, Kalki K, et al. Attenuation correction of SPECT using x-ray CT on an emission-transmission CT system: myocardial perfusion assessment. *IEEE Trans Nucl Sci.* 1996;43:2263–2274.
9. Tang HR, Brown JK, Da Silva AJ, et al. Implementation of a combined x-ray CT-scintillation camera imaging system for localizing and measuring radionuclide uptake: experiments in phantoms and patients. *IEEE Trans Nucl Sci.* 1999;46:551–557.
10. Shepp LA, Vardi Y. Maximum likelihood reconstruction for emission tomography. *IEEE Trans Med Imag.* 1982;MI-1:113–122.
11. Zeng GL, Gullberg GT. Frequency domain implementation of the three-dimensional geometric point response correction in SPECT imaging. *IEEE Trans Nucl Sci.* 1992;39:1444–1453.
12. Tang HR. *A Combined X-Ray CT-Scintillation Camera System for Measuring Radionuclide Uptake in Tumors* [dissertation]. San Francisco, CA: Joint Graduate Group in Bioengineering, University of California; 1998.
13. Tang HR, Brown JK, Hasegawa BH. Use of x-ray CT-defined regions of interest for the determination of SPECT recovery coefficients. *IEEE Trans Nucl Sci.* 1997;44:1594–1599.
14. Tang HR, Brown JK, Hasegawa BH. Radionuclide measurement using projections of x-ray CT-derived templates onto planar nuclear scans [abstract]. *J Nucl Med.* 1998;39(suppl):98P.
15. Da Silva AJ, Tang HR, Hasegawa BH. Absolute quantitation of myocardial activity in phantoms. *IEEE Trans Nucl Sci.* 1999;46:659–666.
16. Da Silva AJ, Tang HR, Wong KH, Wu MC, Dae MW, Hasegawa BH. Absolute in vivo quantitation of myocardial activity using a combined x-ray CT and SPECT system [abstract]. *J Nucl Med.* 1999;40(suppl):182P.
17. Da Silva AJ, Tang HR, Wong KH, Wu MC, Dae MW, Hasegawa BH. Absolute in vivo quantitation of myocardial activity. *IEEE Trans Nucl Sci.* 2000;47:1093–1098.
18. Mueller-Geartner HW, Links JM, Prince JL, et al. Measurement of radiotracer concentration in brain gray matter using positron emission tomography: MRI-based correction for partial volume effects. *J Cereb Blood Flow Metab.* 1992;12:571–583.
19. Rousset OG, Ma Y, Evans AC. Correction for partial volume effects in PET: principle and validation. *J Nucl Med.* 1998;39:904–911.
20. Formiconi AR. Least squares algorithm for region-of-interest evaluation in emission tomography. *IEEE Trans Med Imag.* 1993;12:90–100.
21. Kessler RM, Ellis JR Jr, Eden M. Analysis of emission tomographic scan data: limitations imposed by resolution and background. *J Comput Assist Tomogr.* 1984;8:514–522.
22. Meltzer CC, Zubieta JK, Links JM, Brakeman P, Stumpf MJ, Frost JJ. MR-based correction of brain PET measurements for heterogeneous gray matter radioactivity distribution. *J Cereb Blood Flow Metab.* 1996;16:650–658.
23. Tang HR, Da Silva AJ, Matthay KK, et al. I-131-MIBG imaging with the UCSF x-ray CT-SPECT system [abstract]. *J Nucl Med.* 1999;40(suppl):282P.